AN OVERVIEW OF PRELIMINARY COMPUTATIONAL AND EXPERIMENTAL RESULTS FOR THE SEMI-SPAN SUPER-SONIC TRANSPORT (S4T) WIND-TUNNEL MODEL

Walter A. Silva[1], Boyd Perry III[1], James R. Florance[1], Mark D. Sanetrik[1], Carol D. Wieseman[1], William L. Stevens[1], Christie J. Funk[1], Jiyoung Hur[2], David M. Christhilf[2], and David A. Coulson[3]

[1]Aeroelasticity Branch
NASA Langley Research Center
Walter.A.Silva@nasa.gov

[2]Lockheed-Martin
Hampton, Virginia 23681-0001

[3]Analytical Services Materials, Inc.
Hampton, Virginia 23681-0001

Abstract: A summary of computational and experimental aeroelastic and aeroservoelastic (ASE) results for the Semi-Span Super-Sonic Transport (S4T) wind-tunnel model is presented. A broad range of analyses and multiple ASE wind-tunnel tests of the S4T have been performed in support of the ASE element in the Supersonics Program, part of NASA's Fundamental Aeronautics Program. The computational results to be presented include linear aeroelastic and ASE analyses, nonlinear aeroelastic analyses using an aeroelastic CFD code, and rapid aeroelastic analyses using CFD-based reduced-order models (ROMs). Experimental results from two closed-loop wind-tunnel tests performed at NASA Langley's Transonic Dynamics Tunnel (TDT) will be presented as well.

1 INTRODUCTION

The unique structural configuration of supersonic aircraft combined with nonlinear aerodynamics and rigid-body effects often results in highly complex nonlinear aeroelastic/flight dynamics phenomena. These aeroelastic phenomena can affect ride quality, gust loads, flutter, flight dynamics and control, and engine performance. The aeroelastic/flight dynamics phenomena simultaneously influence the airframe and propulsion system controls, producing undesirable effects on performance and flying characteristics.

These aeroservoelastic (ASE) phenomena need to be thoroughly understood in order for supersonic flight to be safe, efficient, and comfortable. In addition, there is an opportunity, through active controls, to exploit these phenomena for improved performance and efficiency. Analysis and design capabilities for slender supersonic aircraft may then be enhanced by including this new knowledge.

A vast body of analytical, computational, wind-tunnel and flight data exist on the ASE characteristics of subsonic transport and supersonic fighter aircraft [1]. Systems for control of undesirable aeroelastic phenomena, such as suppression of flutter, have been demonstrated in the past [2–5]. Systems that exploit vehicle flexibility for improved performance,

such as vehicle roll control beyond aileron reversal and wing load alleviation have also been demonstrated [6, 7].

Considerably less data are available for supersonic cruise configurations. In the mid- to late-1990s, as part of the High Speed Research (HSR) program, research was performed in the areas of computational and experimental aeroelasticity [8]. As part of this research, aeroelastic wind-tunnel models were designed, built, and tested in the Transonic Dynamics Tunnel (TDT). A remnant from the HSR program is the Semi-Span Super-Sonic Transport (S4T) [9], a very sophisticated, aeroelastically-scaled semispan wind-tunnel model based on the Technology Concept Aircraft (TCA) configuration equipped with three active surfaces (ride control vane, aileron, horizontal tail) and flow-through nacelles with flexible mounts. The model was designed so that it would flutter within the TDT operating boundary, making it an ideal testbed for investigating ASE issues associated with supersonic cruise configurations.

Under the auspices of the Supersonics Project under NASA's Fundamental Aeronautics Program (FAP), the S4T was the subject of four experiments in the TDT: two open-loop (no feedback control) tests and two closed-loop (with feedback control) tests over the span of three years between 2007 and 2010. A special session on the various aspects of the S4T program is being organized for the AIAA Structures, Structural Dynamics, and Materials (SDM) conference to be held in 2012.

The paper begins with a brief description of the S4T wind-tunnel model. Details regarding TDT are available in the references [9]. A description of the Computational Aeroelastic Models is then provided including linear and CFD models. Computational and experimental results are then presented in the Results section of the paper, followed by some Concluding Remarks.

2 WIND-TUNNEL MODEL

2.1 Overall Description

The S4T is a sophisticated aeroelastic semispan wind-tunnel model designed and fabricated at NASA Langley with siginficant contributions from Boeing during the HSR program. The model is shown in Figure 1 mounted on a backstop in a model preparation area at the TDT in two different states of assembly. The photograph on the left of Figure 1 shows the model fully assembled as it would be in the tunnel. The photograph on the right of Figure 1 shows the model without the fuselage fairing installed and with key features highlighted. Those features are the three active surfaces (ride control vane, aileron, horizontal tail), flow-through nacelles with flexible attachments, and the flexible fuselage beam. The engine nacelles include provisions for varying their masses and mount stiffnesses thereby allowing researchers to vary the test conditions at which flutter occurs. It is important to point out that the fuselage fairing (seen on the left of Figure 1) serves only as a rigid aerodynamic shell, is not instrumented in any way, and is non-metric. The flexible fuselage beam has the freedom to move inside the rigid fuselage fairing. As the RCV, wing, and horizontal tail are attached to the flexible fuselage beam, these components also have the freedom to move. The lifting surfaces (RCV, wing, and horizontal tail) protrude from the flexible fuselage beam and pass through gaps on the rigid fuselage fairing. An important aspect during wind-tunnel testing was to ensure that the lifting
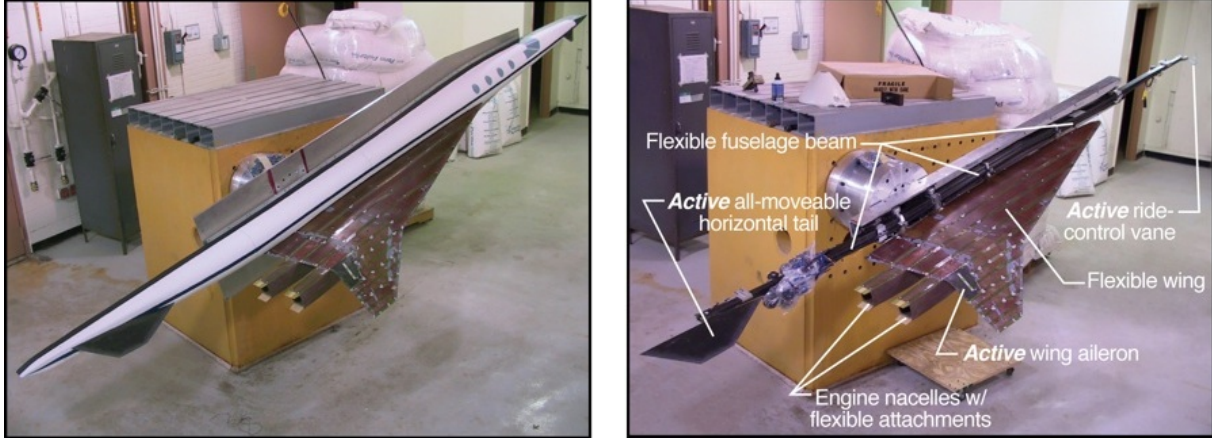
(a) Fully assembled model.   (b) Model without fuselage fairing installed.

Figure 1: Photographs of S4T wind-tunnel model mounted on backstop.

surfaces (metric) were able to move freely within the rigid fuselage gaps and thus did not make contact with the rigid fuselage fairing (non-metric). These gaps were also modeled into the motion of the CFD grid in order to more realistically model the configuration as will be discussed later.

The wind-tunnel model is 16.5 feet in length with a model span of 3.25 feet. The fuselage consists of a graphite-epoxy flexible beam (Figure 2) attached to an aluminum C-channel rigid beam and surrounded by a fiberglass-over-honeycomb fairing. Attachment points allow pitch and vertical motion of the flexible beam (along with minimal fore-aft motion) but constrain roll, yaw, and side motion. Two nodal mounts supply vertical stiffness through four U-springs (two springs per mount) shown in Figure 2. These nodal mounts can be locked with expansion spacers placed between the stop spacers on the U-springs for testing if a nearly cantilevered boundary condition is desired.

The all movable ride control vane (RCV) and horizontal tail are mounted to the flexible beam. Linear piston hydraulic actuators are used to deflect these control surfaces. The horizontal tail assembly is similar to the RCV assembly. Both surfaces have a peak-to-peak range of 30 degrees (+15 to -15).
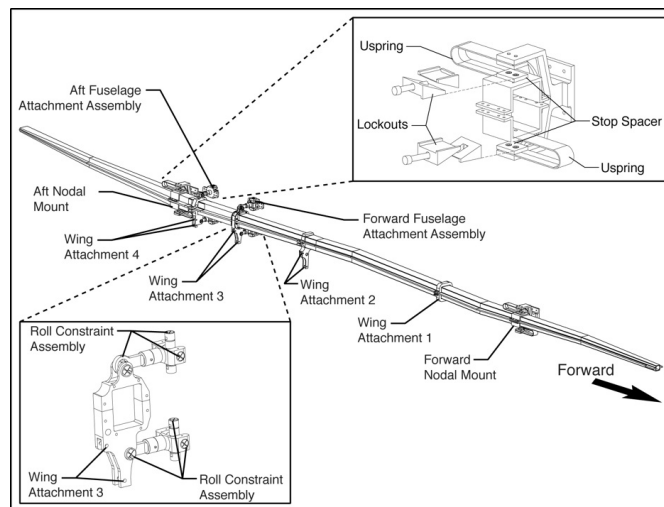

Figure 2: Fuselage beam showing attachment points and nodal mounts.

The wing consists of a fiberglass-epoxy skin over a honeycomb core and has a remotely controlled aileron outboard of the engines. The wing root and tip chords are 82 inches and 6 inches, respectively. The wing attaches to the flexible fuselage beam at four locations through shear pins on the lower and upper surfaces of the wing. The wing's main spar is located between the aft two attachment points and runs out spanwise to the wing tip. The aileron is constructed of graphite-epoxy skins over a honeycomb core and a balsa leading edge. A vane-type hydraulic actuator is used to deflect the aileron through a peak-to-peak range of 5 degrees (+2.5 to -2.5).

2.2 Instrumentation and Related Components

The instrumentation in the wing, illustrated in Figure 3, is extensive. The wing is populated with 26 accelerometers, the engines with four each, and the fuselage with four. In addition, there are 93 unsteady pressure transducers on the wing (53 on the upper surface and 40 on the lower surface) arranged in six chordwise rows, 12 strain gages (bending and torsion gages at three locations on the upper and lower surface), and additional torsional strain gages that measure ride-control-vane, aileron, and horizontal-tail positions. The flexible fuselage beam is instrumented with four accelerometers. The three servovalves (one for each control surface actuator) were mounted on the flexible fuselage. A Q-flex sensor was used to measure angle of attack. A 5-component sidewall balance (TDT-05S) was used to measure loads on only those components of the model shown in Figure ??. That is, the fuselage fairing in non-metric. Figure 4 contains the distribution of the wing pressure transducers with the left side of the figure corresponding to the upper surface and the right side of the figure corresponding to the lower surface. Volume constraints precluded the placement of pressure transducers and accelerometers at the leading and trailing edges of the outboard wing section.
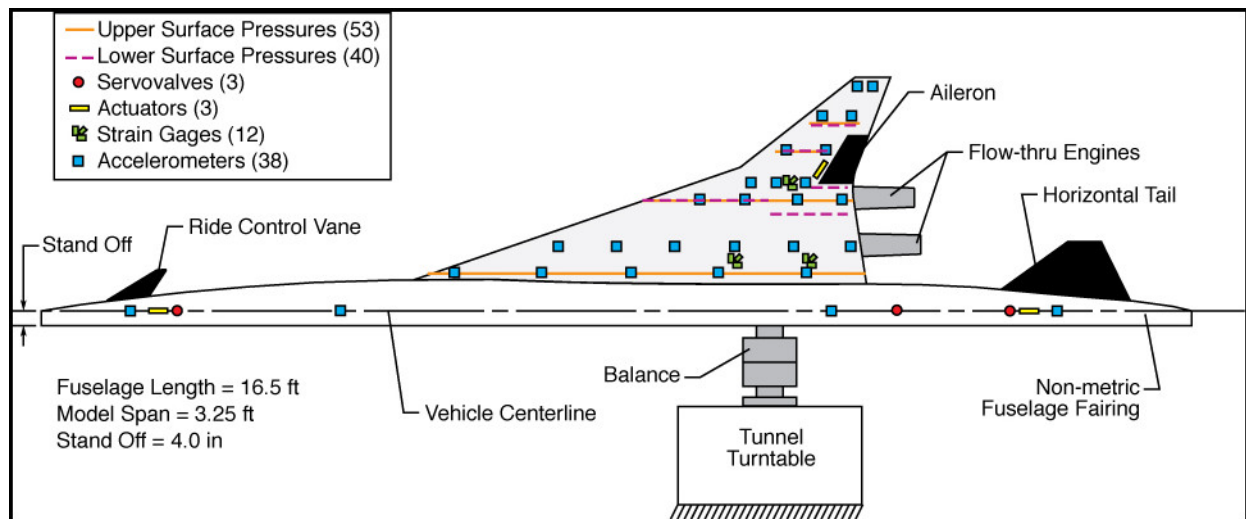

Figure 3: Model instrumentation layout.

3 WIND-TUNNEL MODEL CHARACTERIZATION

Several types of characterization measurements and tests on the wind-tunnel model were conducted prior to all four tests in the TDT. These tests included mass and stiffness measurements, modal surveys on major model components and the fully assembled configuration, model geometry measurements, and actuator frequency response measurements.
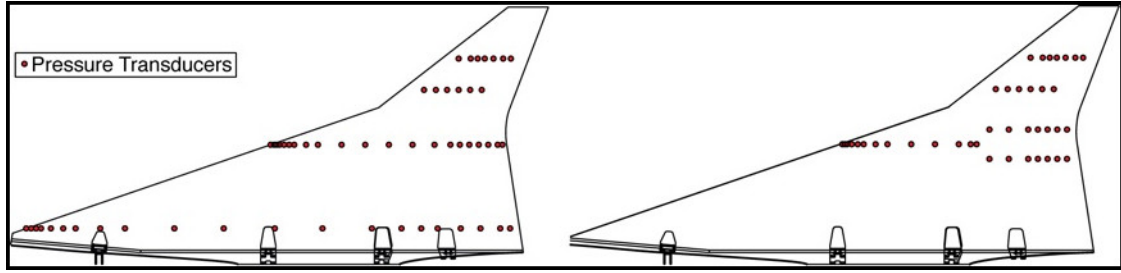
Figure 4: Wing unsteady pressure transducer locations; Left is upper surface, Right is lower surface.

The results from these characterization tests were used for correlation with results from analysis. Where significant differences between measurement and prediction were identified, the analytical representations of the physical model were corrected.

3.1 Stiffness of Wing and Fuselage Beam

The stiffnesses of the wing and flexible fuselage beam were determined by measuring static deflections for various loading conditions. Wing stiffness was determined by applying point loads along the front and rear spars of the outboard wing and measuring the wing deflection using a video model deformation (VMD) system [10]. Sample plots of the measured bending deflection results are presented in the reference by Perry et al [9].

The stiffness of the flexible fuselage beam was determined by applying moments at three locations (the RCV shaft, the second downstream wing attachment point, and the horizontal tail shaft) separately and measuring the angle of deflection along the beam using a calibrated angle measurement system.

3.2 Modal Surveys

Multiple modal surveys, or ground vibration tests (GVTs), were performed as an important component of each wind-tunnel test. Typically, one GVT was performed prior to every wind-tunnel test followed by another GVT at the end of the wind-tunnel test. Early in the program, a GVT was performed on major components separately such as the wing and the flexible fuselage. The data from these separate component tests were used to update the analytical finite element model (FEM).

Table 1 presents a summary of GVT measurements for the first five modes from the most recent (closed-loop) wind-tunnel test conducted in September of 2010. For the most part, frequencies compare well across the board with some variations in damping. The comparison of measured frequencies with those from the FEM is also good. The FEM is discussed in the next section of this paper.

Presented in Figure 5, Figure 6, and Figure 7 are the first three measured flexible modes. The first mode is predominantly a pitch mode about the forward nodal mount; the second mode is predominantly a pitch mode about the balance; and the third mode is predominantly a fuselage beam first bending. As will be shown in the next section, measured mode shapes compare well with those from the updated FEM.

| | Pre-Test in Lab | | Pre-Test in TDT | | Post-Test in TDT | | NASTRAN |
Mode	Frequency	Damping	Frequency	Damping	Frequency	Damping	Frequency
1	6.395	3.547	6.375	5.465	6.249	3.909	6.290
2	8.089	2.285	7.935	2.227	7.838	1.795	8.435
3	10.323	3.518	10.312	2.616	10.059	2.889	10.074
4	11.635	3.745	—	—	11.781	10.903	11.401
5	12.528	1.437	12.585	2.130	12.384	3.224	12.875

Table 1: Measured damping and frequency (Hz) summary and analytical frequencies for most recent wind-tunnel test.
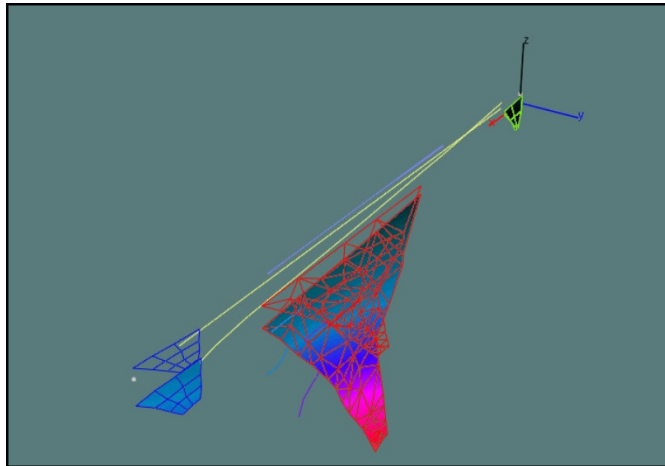

Figure 5: First flexible measured mode (post-test).

4 COMPUTATIONAL AEROELASTIC MODELS

A linear aeroelastic model of the S4T was developed during the initial design of the wind-tunnel model during the HSR program. The structural portion of this linear aeroelastic model is a NASTRAN FEM of the structure consisting of beam and plate representations of 2711 nodes and 4105 elements depicted in Figure 8. The upper and lower surfaces are modeled as plate elements with proper outer mold line geometry definition. The fuselage is modeled as a series of beams and the engines are modeled as simple cruciforms.

The first three flexible modes generated using the final updated NASTRAN FEM are depicted in Figure 9, Figure 10, and Figure 11. The comparison of these analytical modes to the measured modes presented in the previous section is very good.

The aerodynamic portion of the aeroelastic model of the S4T was developed using linear subsonic (doublet lattice) and supersonic (ZONA51) unsteady aerodynamic theories. The aerodynamic box layout is shown in Figure 12.

Computational aeroelastic analyses using higher-order methods were performed for the S4T using the CFL3D structured-grid aeroelastic CFD code using an inviscid and a viscous grid with 7 and 12 million grid points respectively. Both inviscid and viscous solutions were generated at several Mach numbers. Figure 13 presents the viscous surface grid along the symmetry plane. It should be mentioned that initial CFD steady analyses included the engines. However, for aeroelastic analyses, grids were generated without the engines in order to simplify the interpolation of the modes to the gridded engines as well as to reduce the computational time to obtain an aeroelastic solution. Although inclusion of the
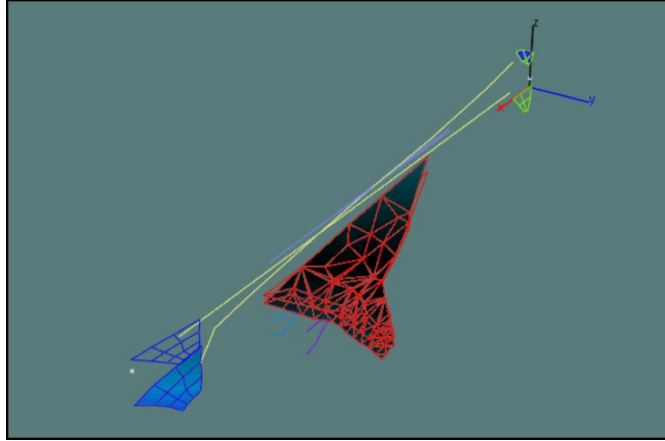
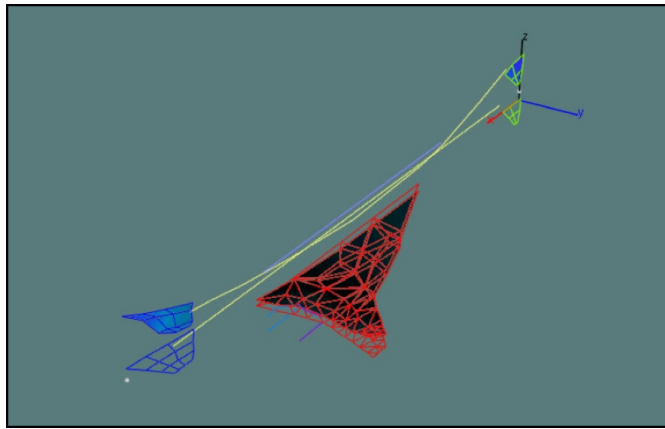Figure 6: Second flexible measured mode (post-test).

Figure 7: Third flexible measured mode (post-test).

engine aerodynamics slightly affected the steady results, it was assumed that the engine aerodynamics would not have a significant impact on the aeroelastic response. Engine masses and inertias were, of course, included in the computation of the mode shapes.

5 ACTIVE CONTROLS

An important objective of this work was the demonstration of flutter-suppression, gust-load-alleviation, and ride-quality-control control laws, singly and in combination, over a range of Mach numbers and dynamic pressures. Control law designers were free to choose their own design methodologies and employ whatever sensors (accelerometers, strain gages) and active control surfaces (ride control vane, aileron, horizontal tail) they desired. Some initial closed-loop performance goals were defined for each of the active controls functions prior to the first closed-loop test. After subsequent open- and closed-loop testing, some of these goals (or metrics) were altered to assure model safety. The initial goals are described below:

The goal of the flutter-suppression (FS) function was to increase the flutter dynamic pressure by an amount at least 44% above the open-loop flutter dynamic pressure while maintaining adequate relative stability. This minimum increase in dynamic pressure was to have been demonstrated across a range of Mach numbers.
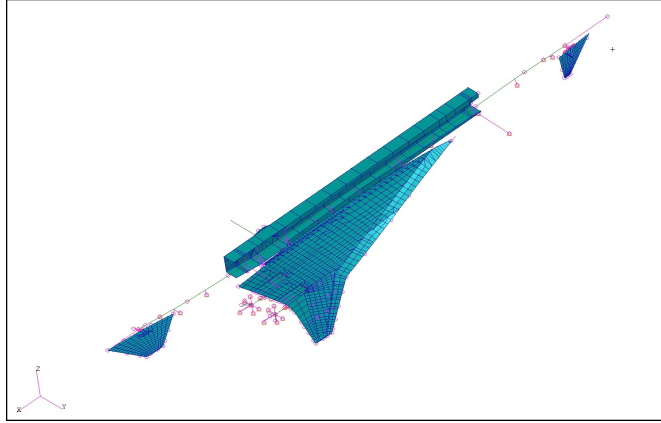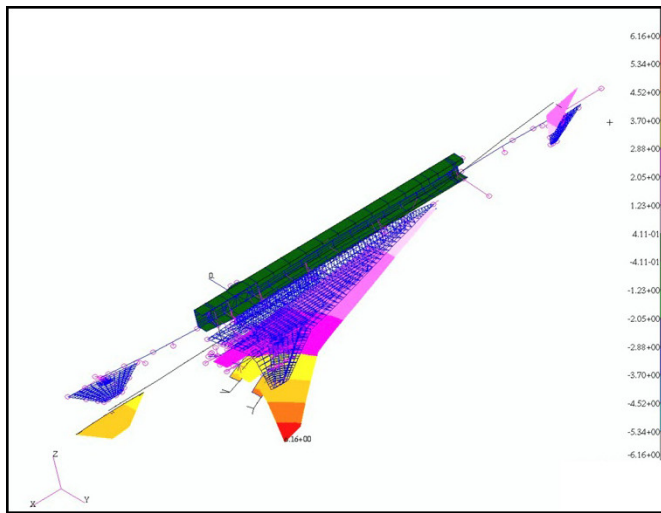
Figure 8: Finite element model.

Figure 9: First flexible analytical mode.

The goal of the gust-load-alleviation (GLA) function was to decrease representative wing-load responses by an amount at least 20% below the open-loop responses while maintaining adequate relative stability. This minimum decrease in loads was to have been demonstrated across a range of Mach numbers. The naturally occurring tunnel turbulence (defined by power spectral density functions) was used as the gust excitation source.

The goal of the ride-quality-enhancement (RQE) function was to decrease representative fuselage acceleration responses by an amount at least 20% below the open-loop responses while maintaining adequate relative stability. This minimum decrease in accelerations was to have been demonstrated across a range of Mach numbers. The naturally occurring tunnel turbulence (defined by power spectral density functions) was used as the gust excitation source.

5.1 Controller Performance Evaluation

During closed-loop testing an online system was employed that provided valuable information about open- and closed-loop stability and performance. The generic name given to this system is controller performance evaluation or CPE [11]. Its open-loop capabilities included verification of the control law loaded into the digital controller and its closed-loop
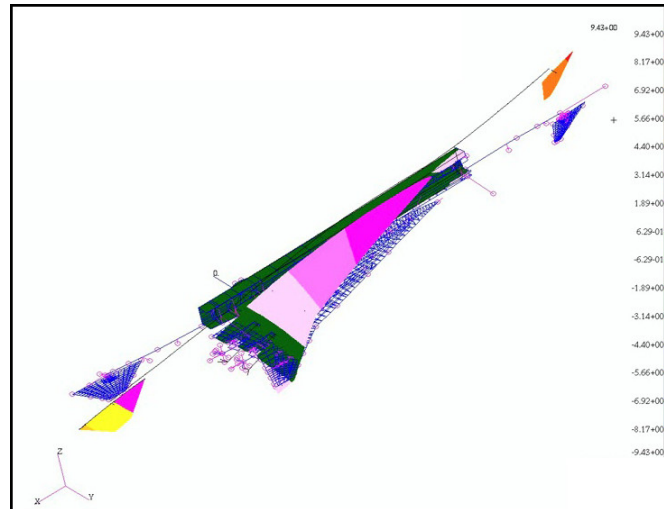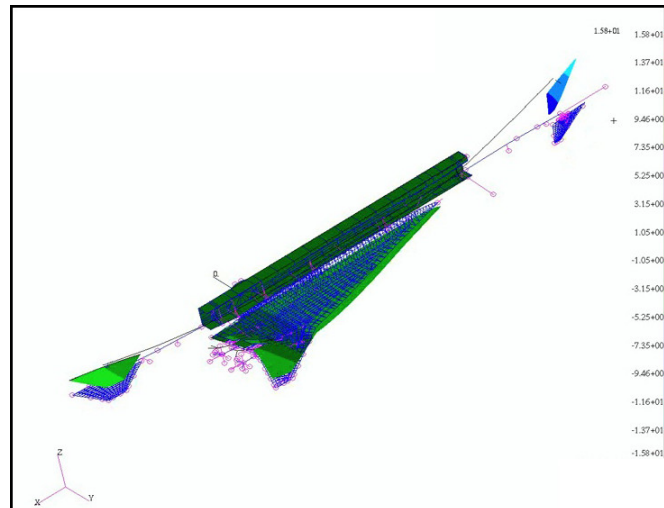
Figure 10: Second flexible analytical mode.

Figure 11: Third flexible analytical mode.

capabilities included prediction of closed-loop system stability. Its closed-loop capabilities included determining the relative stability of a given closed-loop system by evaluating the singular values of the return difference matrices and determining the open-loop plant stability to ascertain the open-loop flutter boundary while operating closed-loop.

5.2 Simulation

A valuable tool that was developed in support of the closed-loop testing was a simulation of the various available S4T plant models and candidate control laws in the Simulink©-based Simulation Architecture for Evaluating Controls for Aerospace Vehicles (SAREC-ASV) [12] simulation framework. A schematic of the various user options available in this tool is presented as Figure 14. The simulation was able to host the discretized state space control laws in a form identical to that used for implementation in the wind tunnel. That capability allowed for screening and enforcement of a standardization of channel sequence, channel names, and physical units.

Candidate excitation signal types, amplitudes and frequency content could be tried in
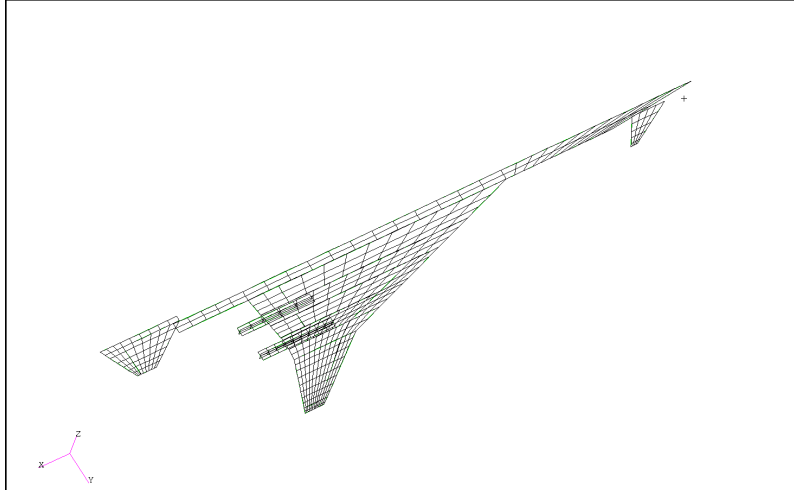
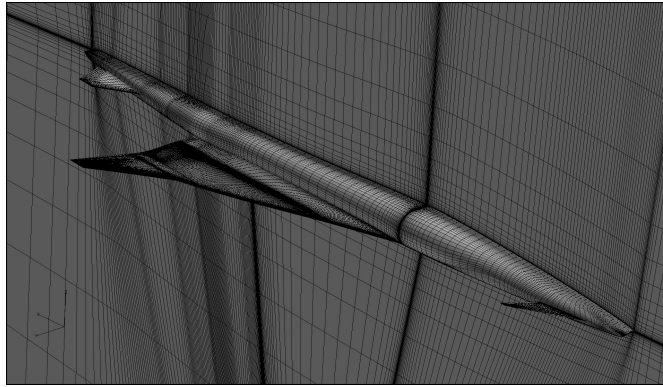Figure 12: Aerodynamic box layout for linear aeroelastic analyses.

Figure 13: Viscous CFL3D surface grid along symmetry plane.

simulation prior to use during wind tunnel testing, and the resulting time histories subjected to the same analysis techniques as were applied to both open- and closed-loop testing in the wind tunnel. Since the simulation for each case that was analyzed was based on a known analytical model, a comparison of frequency responses estimated from time histories, with and without simulated turbulence, was useful for providing pre-test insights with regards to the overall performance of the plant and candidate control law. The Graphical User Interface (GUI) developed for this simulation tool provided a very convenient interface for evaluation of multiple plant models, various turbulence models, and multiple control laws. The simulation was also useful for indicating whether a given control law would have a tendency to reach actuator rate saturation, and possible instability, in the presence of simulated turbulence even for cases that were closed-loop stable and robust according to linear analysis.

6 RESULTS

In this section, a summary of computational and experimental results is provided. The S4T wind-tunnel model was tested four times in the TDT: two open-loop tests and two closed-loop tests. The purpose of the two open-loop tests was to gain familiarity with the model's performance and to acquire system identification data for development of transfer functions to be used subsequently in control law designs. In order to provide a
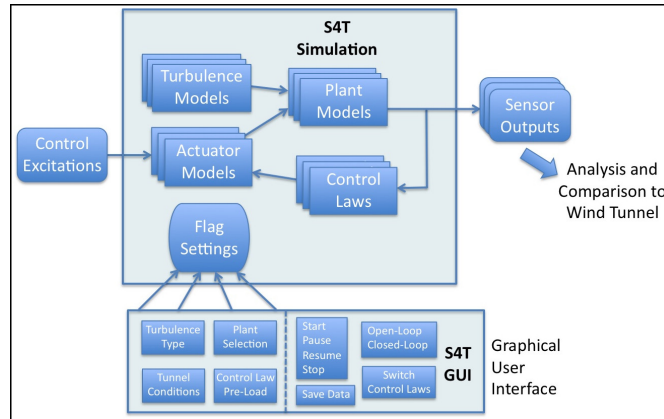
10

Figure 14: Schematic of data flow for the SAREC-ASV simulation tool.

well-defined test plan, it was decided to acquire data and test control laws at three Mach numbers: 0.80, 0.95, and 1.10. Therefore, most of the computational and experimental results to be presented will be at those three Mach numbers.

6.1 Computational Results

Computational results consisted of linear flutter analyses using the NASTRAN model while CFD-based aeroelastic responses and flutter solutions were computed using the CFL3Dv6.4 code [13–15]. The CFL3Dv6.4 code solves the three-dimensional, thin-layer, Reynolds averaged Navier-Stokes equations with an upwind finite volume formulation.
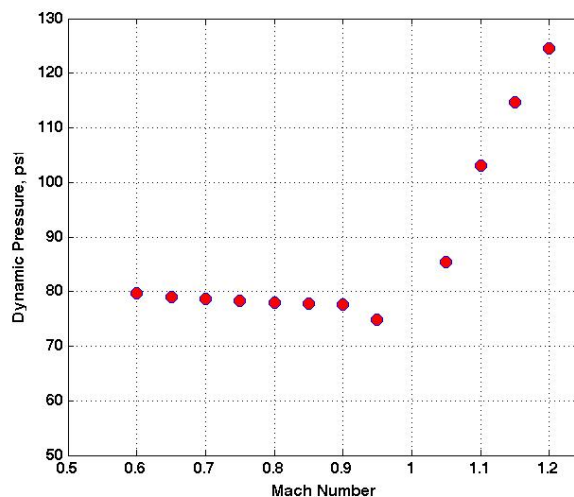

Figure 15: Linear (NASTRAN) flutter dynamic pressure predictions.

Because the CFD and computational structural mechanics (CSM) meshes usually do not match at the interface, CFD/CSM coupling requires a surface spline interpolation between the two domains. The interpolation of CSM mode shapes to CFD surface grid points is done as a preprocessing step. Modal deflections at all CFD surface grids are first generated. Modal data at these points are then segmented based on the splitting of the flow field blocks. Mode shape displacements located at CFD surface grid points of each segment are used in the integration of the generalized modal forces and in the

11

computation of the deflection of the deformed surface. The final surface deformation at each time step is a linear superposition of all the modal deflections.

As previously discussed, the S4T fuselage fairing does not exhibit any motions while the lifting surfaces (RCV, wing, and horizontal tail) are the only surfaces that do exhibit aeroelastic motion. Due to the nature of this configuration, special consideration had to be given to the modal interpolation associated with the interface at the root where the lifting surfaces are in close proximity to the fuselage fairing. As a result, CFD plots and movies will indicate variations and motions only for the three lifting surfaces and none for the fuselage fairing, consistent with the actual wind-tunnel model.

Figure 15 presents the linear (NASTRAN) flutter dynamic pressures for several Mach numbers. Linear results indicate a fairly constant flutter dynamic pressure of about 75 psf for most subsonic Mach numbers with a slight drop around M=0.95 followed by increases in the flutter dynamic pressure at the supersonic Mach numbers. These results are computed with an assumed structural damping of 1%.
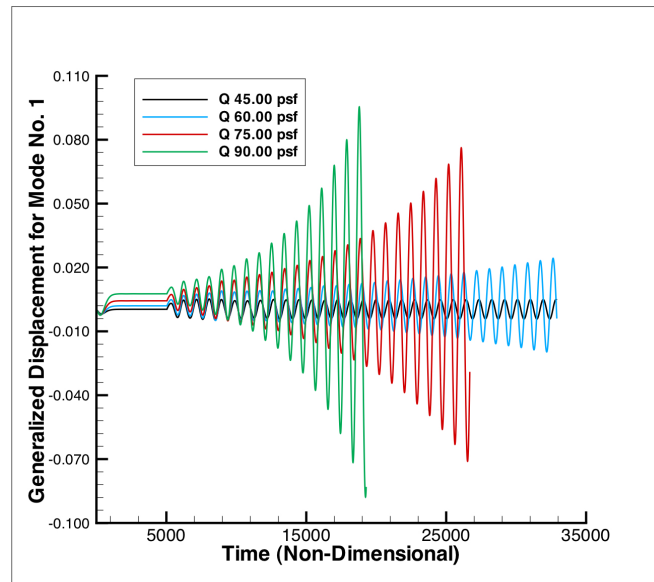

Figure 16: Response of first mode generalized displacement for different dynamic pressures at M=0.95 based on solution of the Euler (inviscid) equations.

A sample of results obtained using the CFL3D code are presented in the following figures [16]. Figure 16 presents the generalized displacement for the first flexible mode at four different dynamic pressures at a Mach number of 0.95 based on solution of the Euler (inviscid) equations. As indicated, the inviscid solution at this Mach number is neutrally stable at about 45 psf. These results are based on an assumed 1% structural damping. Typically, inviscid CFD solutions yield shocks that are stronger and farther aft than when viscous effects are included. As a result, a steep drop in the flutter dynamic pressure for inviscid solutions is typical.

Figure 17 presents the generalized displacement for the first flexible mode at four different dynamic pressures at a Mach number of 0.95 based on solution of Navier-Stokes (viscous) equations. As would be expected, the inclusion of viscosity increases the flutter dynamic pressure over that from the inviscid solution.
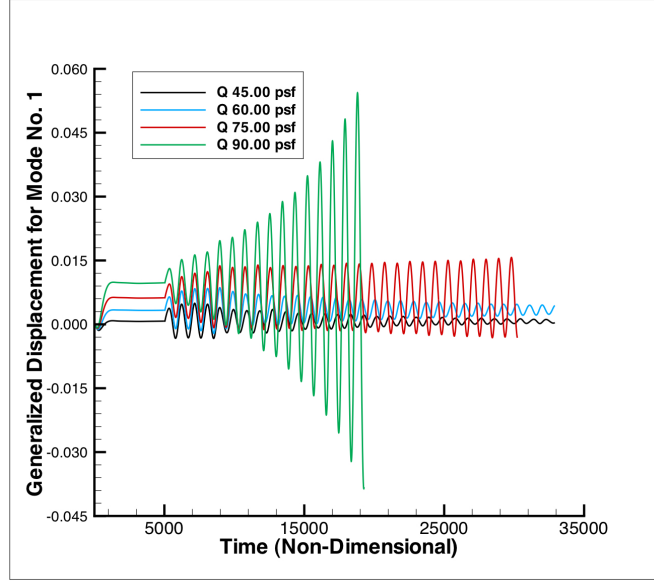
12

Figure 17: Response of first mode generalized displacement for different dynamic pressures at M=0.95 based on solution of the Navier-Stokes (viscous) equations.

Various sensitivity analyses were performed using the CFL3D code. One of those sensitivity analyses was the effect of angle of attack on the aeroelastic stability at a Mach number of 0.95 and a flutter dynamic pressure of 60 psf. Although not shown in this paper, a decrease in the angle of attack, especially near zero and at the negative angles of attack, resulted in decreased aeroelastic stability. As a result, some computational difficulties were encountered when computing aeroelastic responses at zero and negative angles of attack. Additional analyses are currently underway. Details are presented in the references [16].

Mach No.	0.80	0.95	1.10
Linear	78.0	75.0	103.0
CFL3D Inviscid	75.0	45.0	125.0
CFL3D Viscous	82.5	80.0	120.0

Table 2: Predicted Flutter Dynamic Pressures (psf), 1% Structural Damping

Mach No.	0.80	0.95	1.10
Linear	87.0	87.0	119.0
CFL3D Viscous	91.0	89.0	—
Experiment	93.0	91.75	—

Table 3: Flutter Dynamic Pressures (psf), GVT Measured Structural Damping

Presented in Table 2 are the flutter dynamic pressures for the three Mach numbers at which data was acquired (0.8, 0.95, and 1.10) for the Linear, CFL3D Inviscid, and CFL3D Viscous solutions, all with an assumed 1% structural damping. As presented previously, the linear flutter predictions indicate an almost constant flutter dynamic pressure across the subsonic Mach numbers with a rise in the flutter dynamic pressure at supersonic Mach numbers. Likewise the CFL3D Viscous solution indicates a similar trend while the CFL3D Inviscid solution exhibits an unrealistically low flutter dynamic pressure at M=0.95.

13

Recent additional CFL3D analyses performed at other Mach numbers have not yet identified a clear transonic flutter dip. Prior experience [8] has indicated that supersonic configurations, by design, tend to have a very narrow transonic range which can lead to a very narrow ("chimney") transonic flutter dip. Additional analyses are currently underway to see if such a boundary is characteristic of the S4T wind-tunnel model.
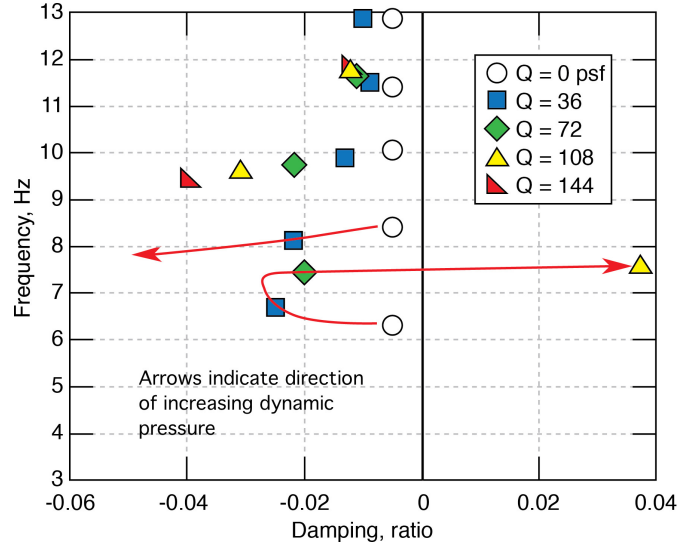

Figure 18: Root locus plot from aeroelastic ROM analysis, M=0.80, one-percent structural damping.

Updated flutter dynamic pressures using measured damping values from a post-test GVT are presented in Table 3 for Linear computations, CFL3D Viscous computations, and Experiment (TDT Test 616). The CFL3D Viscous computations for a Mach number of 1.10 were still underway as of the writing of this paper. Experimental identification of a flutter dynamic pressure at the supersonic Mach number was not possible during the test. This issue is discussed in the next section of the paper.

Development of aeroelastic reduced-order models (ROMs) was performed using CFL3D viscous solutions [17, 18]. These ROMs can be used within a MATLAB/SIMULINK environment to create root locus plots that exhibit the migration of the aeroelastic roots. Presented in Figure 18 is a root locus plot at a Mach number of 0.80 indicating the coalescence of the first and second modes leading to flutter at a dynamic pressure of 78 psf (0.54 psi) with an assumed 1% structural damping. Comparison of the ROM result with that from the full CFL3D viscous solution is very good. Development of ROMs at additional Mach numbers is currently underway.

6.2 Experimental Results

In this section, experimental results from both closed-loop tests are briefly presented. Details regarding control law designs and performance (including control power and actuator activity) are provided in the references [19–26].

Although closed-loop testing of the S4T yielded large amounts of valuable data and experience, it was difficult to meet the proposed closed-loop goals originally stated. As testing experience was gained, it became very obvious that model safety had to take priority over meeting initial closed-loop goals. That is, in several instances during closed-loop testing,
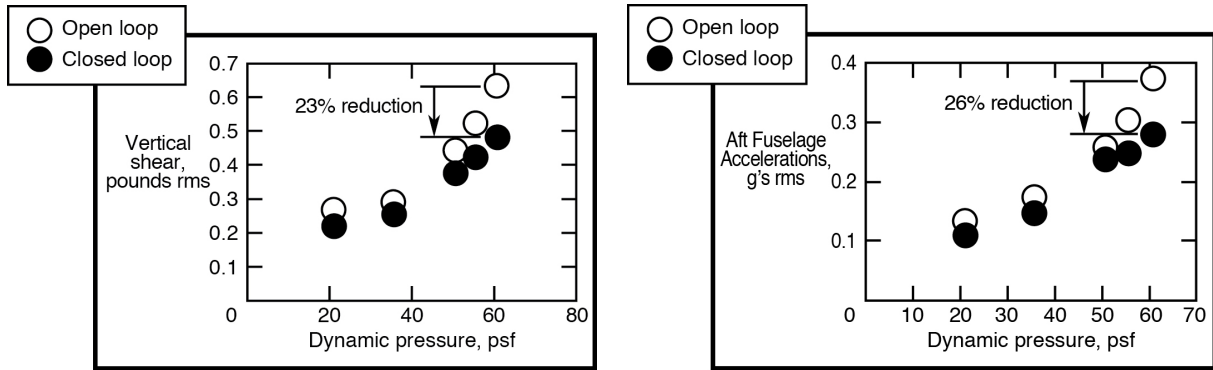
(a) Gust load alleviation (GLA) control law.   (b) Ride quality enhancement (RQE) control law.

Figure 19: Measured responses at M=0.80.

it would have been possible to push a particular control law beyond a flight condition in order to achieve the initial goals. However, the complexity of the S4T model, in particular its control surfaces and actuators, made it clear to the entire test team that any attempt to reach the initial goals would endanger the safety of the model. These model safety limitations included measured closed-loop gains, minimum singular values, and overall motion of the model. This safety-minded approach, however, is consistent with the initial goals that included the requirement to "maintain adequate relative stability".

One important closed-loop goal that was achieved was to be able to perform multiple control modes (Gust Load Alleviation (GLA), Ride Quality Enhancement (RQE), and Flutter Suppression (FS)) simultaneously. Several control laws were designed specifically to perform in this fashion and did so successfully. In terms of GLA, a sample result from the first closed-loop test is presented on the left figure of Figure 19 as vertical shear versus dynamic pressure for open- and closed-loop measurements. The vertical shear was computed from a calibration of the wing's strain gauges. As can be seen, for this particular GLA control law, the measured vertical shear was reduced by 23% at the highest dynamic pressure.

Similarly, a sample result from the first closed-loop test for RQE is presented on the right figure in Figure 19 as aft fuselage acceleration versus dynamic pressure for open- and closed-loop measurements. As shown in the figure, a 26% reduction in the aft fuselage acceleration was achieved at the highest dynamic pressure tested (60 psf). For this particular condition and control law, the goal of a reduction in wing load responses by at least 20% was achieved while maintaining adequate relative stability.

The focus of the first closed-loop test was on the validation of GLA and RQE control laws. Although some FS was attempted during this test, there was not enough time to carry out this phase of testing in a safe manner. Therefore, the second closed-loop test was focused on FS only. In order to perform FS safely, the CPE method described previously was used to identify an open-loop instability while the model was closed-loop stable. This was performed using Nyquist stability criteria.

Nyquist stability criteria, as represented by Nyquist plots, enables the identification of an open-loop instability using data acquired while the model is closed-loop stable. This provided a very safe method for identifying the open-loop flutter dynamic pressures as the actual encounter of a potentially destructive flutter point was avoided. Presented in
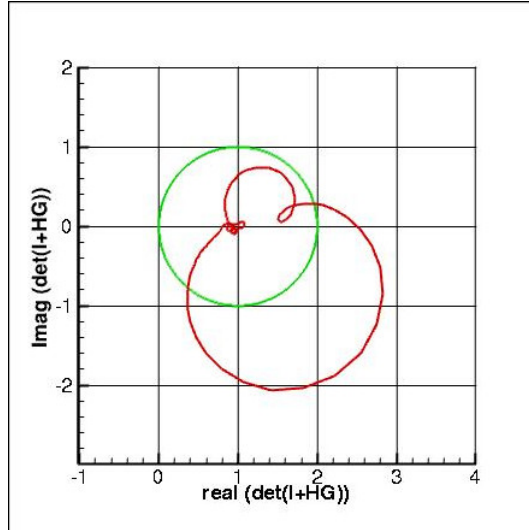
Figure 20: Nyquist plot at Mach number 0.80 and a dynamic pressure of 79 psf.
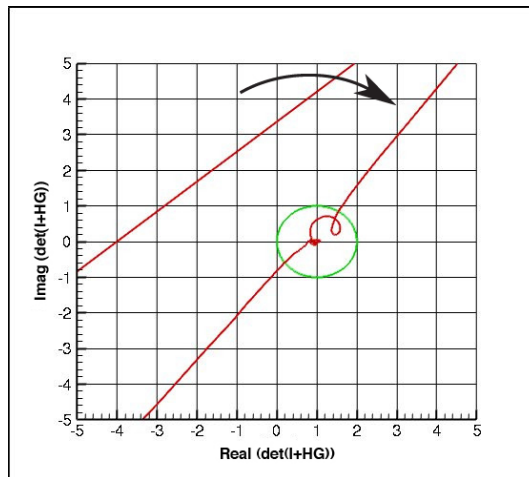

Figure 21: Nyquist plot, Mach number of 0.80 and a dynamic pressure of 89 psf.

Figure 20 is a Nyquist plot acquired from the simulated closed-loop system at M=0.80 and a dynamic pressure below the open-loop flutter point. As can be seen, there are no encirclements of the origin, indicating a stable open-loop system. It can be seen, however, that an encirclement may be approaching.

Figure 21 presents a simulated Nyquist plot at an even higher dynamic pressure clearly showing an encirclement, indicating that the system is no longer open-loop stable. During the test, however, Nyquist plots were generated based on measured data. The information gleaned from those plots was used to make decisions whether to continue increasing dynamic pressure. Due to limited space, samples of those plots are not presented in this paper.

Presented in Figure 22 is a plot of flutter dynamic pressure versus Mach number with the flutter dynamic pressures identified for Mach numbers of 0.80 and 0.95 using the Nyquist method described above. With the system closed-loop stable, a dynamic pressure of 95 psf was reached. Analysis of Nyquist plots indicated an open-loop instability of 93 psf for Mach number of 0.80 and 91.75 for Mach number of 0.95. Also presented in the

16

plot is the highest attainable dynamic pressure of about 110 psf at Mach number of 1.10 that was reached with the system closed-loop stable. Based on the lack of an open-loop encirclement up to this dynamic pressure, the indication is that the open-loop flutter point at this Mach number is above the 110 psf condition. Again, due to model safety concerns, it was decided not to go beyond the 110 psf in order to find the open-loop flutter point. The primary concern at this condition is the possible existence of a transonic flutter dip somewhere between a Mach number of 0.95 and 1.10. If so, then due to the nature of TDT operations, a region of high instability could be encountered on the way back down from Mach number of 1.10 for a dynamic pressure higher than the 110 psf. For this reason, the identification of the open-loop flutter point at a higher dynamic pressure was not pursued.
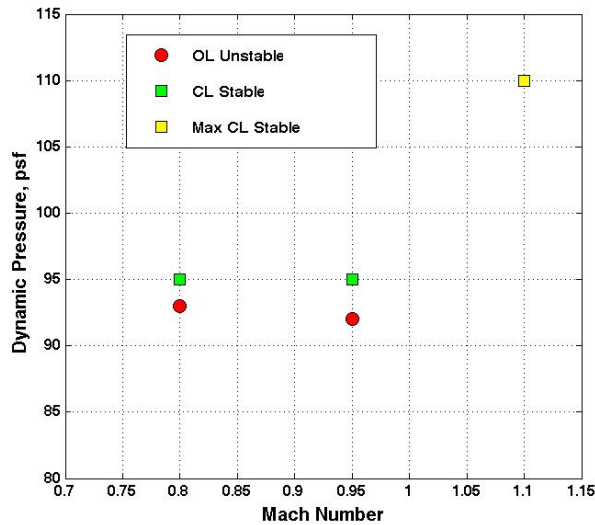

Figure 22: Identification of open-loop flutter dynamic pressures for Mach numbers of 0.80, 0.95, and 1.10.

7 CONCLUDING REMARKS

A brief summary of computational and experimental results were presented for the SemiSpan SuperSonic Transport (S4T) wind-tunnel model tested in the Transonic Dynamics Tunnel on four different occasions (two open-loop tests, two closed-loop tests) between 2007 and 2010. A description of the wind-tunnel model including primary hardware and associated test hardware was provided including a description of the digital control system, a closed-loop simulation tool, and the controller performance evaluation (CPE) system. Computational results included linear aeroelastic analyses using NASTRAN and nonlinear aeroelastic responses using the CFL3D aeroelastic code. Also presented was a sample root locus result obtained from the application of reduced-order modeling (ROM) methods developed at NASA. The experimental results presented included samples of results from evaluation of Gust Load Alleviation (GLA), Ride Quality Enhancement (RQE), and Flutter Suppression (FS) control laws. The successful application of an experimental Nyquist stability criterion in order to identify the open-loop flutter points while maintaining closed-loop stability was also presented. An important lesson learned from these analyses and experiments is that the identification of flutter boundaries for supersonic configurations may be elusive. That is, although linear and nonlinear analyses presented similar flutter boundary trends, a transonic flutter dip has not been identified to date. If, based on prior experience, this transonic flutter dip is very narrow, it could pose a

hidden and serious risk within the flight envelope. Additional analyses and experiments are certainly required to completely understand the aeroelastic response of supersonic configurations.

8 REFERENCES

[1] "Advanced Aeroservoelastic Testing and Data Analysis," *AGARD Conference Proceedings 566, NATO*, November 1995.

[2] Noll, T. E., "Aeroservoelasticity," *31st AIAA/ASME/ASCE/AHS/ASC Structures, Structural Dynamics and Materials Conference*, No. A90-29359, Long Beach, CA, April 1990.

[3] Sandford, M. C., Abel, I., and Gray, D. L., "Development and Demonstration of a Flutter-Suppression System Using Active Controls," *NASA TR R-450*, 1975.

[4] Abel, I., Perry, B., and Newsom, J. R., "Comparison of Analytical and Wind-Tunnel Results for Flutter and Gust Response of a Transport Wing with Active Controls," *NASA TP 2010*, 1982.

[5] Waszak, M. R., "Robust Multivariable Flutter Suppression for the Benchmark Active Control Technology (BACT) Wind-Tunnel Model," *Eleventh Symposium on Structural Dynamics and Control*, May 12-14 1997.

[6] Multiple, "Special Section: Active Flexible Wing," *Journal of Aircraft*, Vol. 32, January-February 1995.

[7] Pendleton, E. W., Bessette, D., Field, P. B., and Miller, G. D., "Active Aeroelastic Wing Flight Research Program Technical Program and Model Analytical Development," *Journal of Aircraft*, Vol. 37, July-August 2000.

[8] Silva, W. A., Keller, D. F., Florance, J. R., Cole, S. R., and Scott, R. C., "Experimental Steady and Unsteady Aerodynamic and Flutter Results for HSCT Semispan Models," *AIAA/ASME/ASCE/AHS/ASC 41st Structures, Structural Dynamics, and Materials Conference*, No. 2000-1697, April 2000.

[9] Perry, B., Silva, W. A., Florance, J. R., Wieseman, C. D., Pototzky, A. S., Sanetrik, M. D., Scott, R. C., Keller, D. F., Cole, S. R., and Coulson, D. A., "Plans and Status of Wind-Tunnel Testing Employing an Aeroservoelastic Semispan Model," *48th AIAA/ASME/ASCE/AHS/ASC Structures, Structural Dynamics, and Materials Conference*, No. AIAA Paper No. 2007-1770, Honolulu, HI, April 23-26 2007.

[10] Barrows, D., "Videogrammetric Model Deformation Measurement Technique for Wind Tunnel Applications," *45th AIAA Aerospace Sciences Meeting and Exhibit*, Jan. 2007.

[11] Pototzky, A. S., Wieseman, C. D., Hoadley, S. T., and Mukhopadhyay, V., "On-Line Performance Evaluation of Multiloop Digital Control Systems," *Journal of Guidance, Control, and Dynamics*, Vol. 15, July-August 1992, pp. 878–884.

[12] Christhilf, D. M., Pototzky, A. S., and Stevens, W. L., "Incorporation of SemiSpan SuperSonic Transport (S4T) Aeroservoelastic Models into SAREC-ASV Simulation," *AIAA Guidance, Navigation, and Control Conference*, Vol. AIAA-2010-8099, Toronto, CA, Aug. 2010.

[13] Krist, S. L., Biedron, R. T., and Rumsey, C. L., "CFL3D User's Manual Version 5.0," Tech. rep., NASA Langley Research Center, 1997.

[14] Bartels, R. E., "Mesh Strategies for Accurate Computations of Unsteady Spoiler and Aeroelastic Problems," *AIAA Journal of Aircraft*, Vol. 37, 2000, pp. 521–525.

[15] Bartels, R. E., Rumsey, C. L., and Biedron, R. T., "CFL3D Version 6.4: General Usage and Aeroelastic Analysis," *NASA TM 2006 214301*, April 2006.

[16] Hur, J., "Aeroelastic Analysis of SemiSpan SuperSonic Transport (S4T) Wind-Tunnel Model for Transonic Speeds," *NASA CR, In progress*, 2011.

[17] Silva, W. A., "Simultaneous Excitation of Multiple-Input/Multiple-Output CFD-Based Unsteady Aerodynamic Systems," *Journal of Aircraft*, Vol. 45, No. 4, July-August 2008, pp. 1267–1274.

[18] Silva, W. A., "Recent Enhancements to the Development of CFD-Based Aeroelastic Reduced Order Models," *48th AIAA/ASME/ASCE/AHS/ASC Structures, Structural Dynamics, and Materials Conference*, No. AIAA Paper No. 2007-2051, Honolulu, HI, April 23-26 2007.

[19] Roughen, K., Bendiksen, O., and Gadient, R., "Active Aeroelastic Control of the Supersonic Semispan Transport (S4T) Model," *AIAA Guidance, Navigation, and Control Conference*, Vol. AIAA-2010-8397, Toronto, CA, Aug. 2010.

[20] Roughen, K., Bendiksen, O., and Gadient, R., "Active Aeroelastic Control of the Supersonic Semispan Transport (S4T) Model," *51st AIAA Structures, Structural Dynamics, and Materials Conference*, Vol. AIAA-2010-8397, Orlando, FL, April 2010.

[21] Hammerand, D., Gariffo, J., Roughen, K., Baker, M., and Bendiksen, O., "Generation of Aeroservoelastic Reduced Order Models Using Time Scaling," *51st AIAA Structures, Structural Dynamics, and Materials Conference*, Vol. AIAA-2010-2947, Orlando, FL, April 2010.

[22] Roughen, K. and Bendiksen, O., "Development of Generalized Aeroservoelastic Reduced Order Models," *50th AIAA Structures, Structural Dynamics, and Materials Conference*, Vol. AIAA-2009-2491, Palm Springs, CA, April 2009.

[23] Roughen, K., "Active Aeroelastic Control of Supersonic Transport Aircraft," *PhD Dissertation*, University of California, Sept. 2009.

[24] Chen, P. C., Moulin, B., Ritz, E., Lee, D. H., and Zhang, Z., "CFD-Based Aeroservoelastic Control for Supersonic Flutter Suppression, Gust Load Alleviation, and Ride Quality Enhancement," *50th AIAA Structures, Structural Dynamics, and Materials Conference*, Vol. AIAA-2009-2537, Palm Springs, CA, April 2009.

[25] Moulin, B., Ritz, E., Chen, P. C., Lee, D. H., and Zhang, Z., "CFD-Based Control for Flutter Suppression, Gust Load Alleviation, and Ride Quality Enhancement for the S4T Model," *51st AIAA Structures, Structural Dynamics, and Materials Conference*, Vol. AIAA-2010-2623, Orlando, FL, April 2010.

[26] Moulin, B., Ritz, E., Florance, J. R., Sanetrik, M. D., and Silva, W. A., "CFD-Based Classic and Robust Aeroservoelastic Control for the SuperSonic SemiSpan Transport Wind-Tunnel Model," *AIAA Guidance, Navigation, and Control Conference*, Vol. AIAA-2010-7802, Toronto, CA, Aug. 2010.